Chinese Physics Letters **xx**, xxxxxx (2026) **New Submission**

Theoretical prediction of superconductivity and nontrivial band topology in rock-salt transition-metal hydrides MH (M = Mo, W, Ru, Rh, Y)

Yan-Li Zhang (张艳丽)[1], Hao Ding (丁豪)[1], Han Wang (王菡)[1], Ya-Ping Li (李牙平)[1], Jin-Han Tan (谭锦函)[1], Na Jiao (焦娜)[1,*], Rui Wang (王锐)[2,3,4,*], and Hong-Yan Lu (路洪艳)[1,*]

[1]*School of Physics and Physical Engineering, Qufu Normal University, Qufu 273165, China*
[2]*National Laboratory of Solid State Microstructures and Department of Physics, Nanjing University, Nanjing 210093, China*
[3]*Collaborative Innovation Center of Advanced Microstructures, Nanjing University, Nanjing 210093, China*
[4]*Jiangsu Physical Science Research Center, Nanjing 210093, China*

(Received xxx; accepted manuscript online xxx)

Transition-metal hydrides have recently emerged as a promising platform for exploring the interplay between superconductivity and nontrivial band topology. Here, using first-principles calculations, we predict a family of rock-salt transition-metal monohydrides MH (M = Mo, W, Ru, Rh, Y) that are stable at ambient pressure. Our calculations show that these compounds exhibit phonon-mediated superconductivity, with estimated superconducting transition temperatures of 14.6 K, 14.5 K, 5.3 K, 7.9 K, and 4.5 K for MoH, WH, RuH, RhH, and YH, respectively. For MoH and WH, the electron-phonon coupling is mainly contributed by the softened low-frequency phonon modes associated with transition-metal vibrations, which couple strongly to the doubly degenerate d-orbitals ($d_{x^2-y^2}$ and d_{z^2}) near the Fermi level. In addition, spin-orbit coupling opens nontrivial band gaps near the Fermi level, as confirmed by $\mathbb{Z}_2$ topological invariants and topologically protected surface states. These results identify rock-salt transition-metal monohydrides as promising ambient-pressure platforms for investigating the coexistence of superconductivity and nontrivial band topology.

Keywords: transition-metal hydrides; electron-phonon coupling; superconductivity; nontrivial band topology

DOI: 10.1088/0256-307X/xx/x/xxxxxx

Introduction. The exploration of materials with both topological and superconducting properties has received widespread attention in condensed matter physics. Notably, the rock-salt type structure (space group Fm-3m) has shown unique advantages in the study of superconductivity and topological states in recent years [1–3]. Its cubic symmetry leads to the degeneracy of electronic energy bands on high symmetry lines, which provide for the formation of various topological semimetallic states, such as Dirac points [4–7], Weyl points [8,9], or nodal lines [10,11]. It should be noted that the rock-salt structure itself provides a symmetry basis for the formation of topological states, and when the system contains transition-metal elements, the d-electrons of transition-metals have multiple orbital degrees of freedom, which greatly enriches the sources of band degeneracy and provides more possibilities for the formation of degeneracy points protected by symmetry. For example, rock-salt transition-metal carbides NbC [12,13] and TaC [13,14] exhibit three closed nodal lines, which are protected by time and space inversion symmetry. Meanwhile, they also display superconductivity with superconducting transition temperature (T_c) of 11.5 K and 10.3 K, respectively. In addition, the high symmetry of rock-salt structure combined with transition-metal d-electrons can help improve superconducting performance, because d-electrons of transition-metals contribute high electron density of states near the Fermi level, enhancing the electron-phonon coupling (EPC) through strong electron correlation, and thus lead to higher T_c. For example, the α-MoC [15] and δ-NbN [16] with rock-salt structure exhibit both topological nontrivial electronic structure characteristics and excellent superconducting properties, with T_c of 24.7 K and 18.2 K, respectively. Therefore, the search for more rock-salt type transition-metal compounds with topology and superconductivity has attracted widespread attention.

According to the BCS theory, the T_c is positively correlated with the logarithmic average of the phonon frequencies [17–19]. The small mass of hydrogen atoms makes their phonon frequency much higher than that of other elements. In addition, hydrogen may promote and enhance coupling between other elements. Therefore, hydrides undoubtedly play a crucial role in the exploration of high-temperature superconductors [20–24]. Meanwhile, in hydrides formed under high pressure, the high-frequency vibrations of the hydrogen lattice can effectively mediate the electron phonon attraction, resulting in extremely strong EPC [25], which is a key mechanism for achieving high-temperature or even room temperature superconductivity. Many hydride superconductors have been theoretically predicted and synthesized, such as H_3S (T_c = 203 K at 155 GPa) [26–28], LaH_{10} (T_c = 250 K at 170 GPa) [29–34], and YH_6 (T_c = 224 K at 166 GPa) [34–36]. This is a direct manifestation of the excellent charac-

*Corresponding authors. Email: j_n2013@126.com; rwang89@nju.edu.cn; hylu@qfnu.edu.cn
© 2026 Chinese Physical Society and IOP Publishing Ltd

teristics of hydrides. The research on hydrides under high pressure is very rich, while there is relatively little research on ambient pressure hydrides that possess both topological and superconducting properties. For example, several ambient-pressure hydride superconductors have been theoretically studied, such as LuH [37] and MH_4 [38], but they only exhibit traditional superconducting behavior and lack extraordinary topological electronic structures. Therefore, exploring the coexistence of topology and superconductivity in hydrides under ambient pressure is of great significance.

In this work, using first-principles calculations, we predict a family of ambient-pressure stable rock-salt transition-metal monohydrides MH (M = Mo, W, Ru, Rh, Y). They exhibit phonon-mediated superconductivity with estimated transition temperatures of 14.6 K (MoH), 14.5 K (WH), 5.3 K (RuH), 7.9 K (RhH), and 4.5 K (YH). For MoH and WH, the EPC arises mainly from softened low-frequency phonon modes associated with transition-metal vibrations, which couple strongly to doubly degenerate d-orbitals near the Fermi level. Moreover, spin-orbit coupling opens nontrivial band gaps near the Fermi level, as confirmed by $\mathbb{Z}_2$ topological invariants and topologically protected surface states. Thus, our findings lay a critical theoretical foundation for investigations into rock-salt metal hydrides that exhibit both superconductivity and nontrivial band topology.

Computational Details. All computations presented in this work are based on the density functional theory (DFT). Structural relaxation, electronic band structure and density of states (DOS) for MH (M = Mo, W, Ru, Rh, Y) are calculated using Quantum ESPRESSO [39], while the DOS is also calculated and double confirmed by using Nanodcal [40]. The projector augmented wave (PAW) [41,42] method and the generalized gradient approximation (GGA) with the Perdew-Burke-Ernzerhof (PBE) parameterization [43] are used to simulate electron-ion interactions and exchange-correlation potentials, respectively. During structural optimization, both the lattice parameters and the atomic positions are fully relaxed, with convergence thresholds set at 10^{-7} eV for energy and 0.01 eV/Å for forces. The electronic wave functions of the plane-wave basis and the charge density with energy cutoffs are 80 Ry and 800 Ry, respectively. The EPC are calculated using density functional perturbation theory (DFPT) [44]. The electronic integration is performed over a 16 × 16 × 16 k-point grid. The phonon and EPC are calculated on a 8 × 8 × 8 q-point grid, and a denser 32 × 32 × 32 k-point grid is used for evaluating an accurate electron-phonon interaction matrix. The Coulomb pseudopotential $\mu^* = 0.10$ is adopted in the calculation of the superconducting transition temperature T_c. The topological surface states are calculated by the iterative Green's function method implemented in the WANNIERTOOLS package [45,46], where the basis set is constructed from maximally localized Wannier functions (MLWFs) [47,48] generated by the VASP2WANNIER90 interface [49].

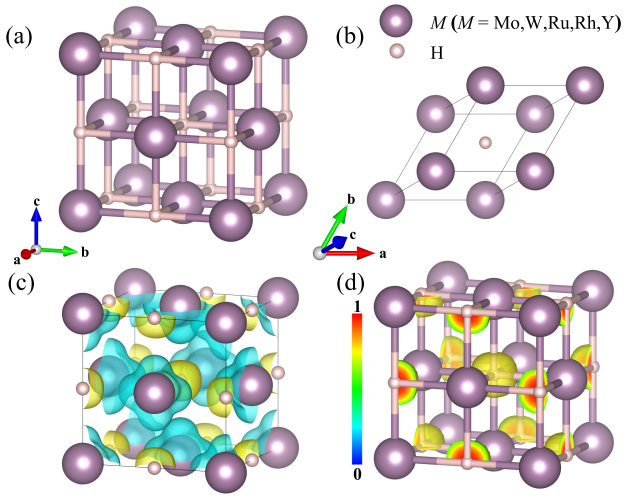

Fig. 1. (a) Unit cell and (b) primitive cell of MH (M = Mo, W, Ru, Rh, Y). (c) The charge density difference of MoH. Blue (yellow) represents the area where electrons are lost (obtained). (d) 3D electron localization function of MoH.

Crystal structures and stability. The unit cell and primitive cell of rock-salt type MH (M = Mo, W, Ru, Rh, Y) are shown in Figs. 1(a) and 1(b), respectively, with the space group of $Fm\bar{3}m$ (No. 225). The crystal structure consists of two interpenetrating face-centered cubic sublattices formed by M (M = Mo, W, Ru, Rh, Y) atoms and H atoms. The transition-metal M (M = Mo, W, Ru, Rh, Y) atoms form a face-centered cubic framework, whereas the H atoms fully occupy all octahedral interstitial sites, namely the edge centers and the body center of the cube. In this structure, each ion lies at the center of an octahedral coordination environment, reflecting the energy minimization tendency toward high symmetry and coordination number under ionic bonding. After structural optimization, the lattice constants of MH (M = Mo, W, Ru, Rh, Y) are shown in Table 1. As the atomic radius of transition-metals increases, their crystal lattice constant a and M (M = Mo, W, Ru, Rh, Y)-H bond $l_{\text{M-H}}$ exhibit a synchronous increasing trend. Among them, Mo and W atoms have similar atomic radii, electronegativity, and valence electron arrangements, so the lattice constants and M-H bond lengths of these two transition-metal hydrides are very close.

The stabilities of MH (M = Mo, W, Ru, Rh, Y) are studied from three aspects: dynamic stability, thermodynamic stability, and mechanical stability. To evaluate dynamic stability, the phonon spectra of the five structures are computed. The phonon spectra of

Table 1. Optimized lattice constant a (Å), bond length l (Å), Formation energy E_{form} (eV/atom), calculated elastic constants C_{ij} (GPa), Young' s modulus E (GPa), bulk modulus B (GPa), shear modulus G (GPa) and Poisson' s ratio ν for MH (M = Mo, W, Ru, Rh, Y).

Material	a	$l_{\text{M-H}}$	E_{form}	C_{11}	C_{12}	C_{44}	E	B	G	ν
MoH	4.08	2.04	-0.397	496.95	150.32	121.19	357.07	265.86	139.90	0.28
WH	4.12	2.06	-0.417	482.16	199.94	159.29	388.42	294.02	151.75	0.28
RhH	3.98	1.99	-0.331	319.46	192.21	58.75	167.53	234.63	60.65	0.38
RuH	3.96	1.98	-0.074	497.36	170.34	162.39	409.03	279.34	162.84	0.26
YH	4.69	2.34	-0.372	127.43	38.95	34.00	95.72	68.44	37.78	0.27

MoH and WH are shown in Figs. 5(a) and 5(e), while the phonon spectra of RuH, RhH, and YH are shown in Fig. S1 (see the Supplemental Material), exhibit no imaginary frequencies across the entire Brillouin zone, indicating that they are dynamically stable. To verify the thermodynamic stability of MH (M = Mo, W, Ru, Rh, Y), the formation energies (E_{form}) of five structures are calculated, as listed in Table 1, using the formula

$$E_{form} = \frac{E_{M\text{H}} - E_M - E_{\text{H}}}{2}, \tag{1}$$

in which $E_{M\text{H}}$, E_M, and E_{H} represent the total energies of MH (M = Mo, W, Ru, Rh, Y), the energy of an atom in M (M = Mo, W, Ru, Rh, Y) element and the energy of an atom in a hydrogen molecule, respectively. To further assess the thermodynamic stability, composition-dependent convex-hull analyses were performed for the Mo–H, W–H, Ru–H, Rh–H, and Y–H systems. As shown in Fig. S9 of the Supplemental Material, MoH, WH, RuH, RhH, and YH are located on the lower convex hulls of their respective binary systems, further supporting their thermodynamic stability at ambient pressure. In addition, the *ab initio* molecular dynamics (AIMD) simulations were performed to examine their finite-temperature structural robustness. The variation of free energy in the AIMD simulations within 15 ps and the last frame of the photographs are shown in Figs. S1 and S2 (see the Supplemental Material). The results show that the crystal framework remains intact throughout the AIMD simulations even at 1000 K, indicating their finite-temperature structural robustness. Finally, their mechanical stability is examined by calculating key elastic parameters, the elastic constants C_{11}, C_{12} and C_{44}, as summarized in Table 1. The elastic constants satisfy the "Born stability criteria" [50], which states that

$$C_{11} > |C_{12}|, C_{11} + 2C_{12} > 0, C_{44} > 0. \tag{2}$$

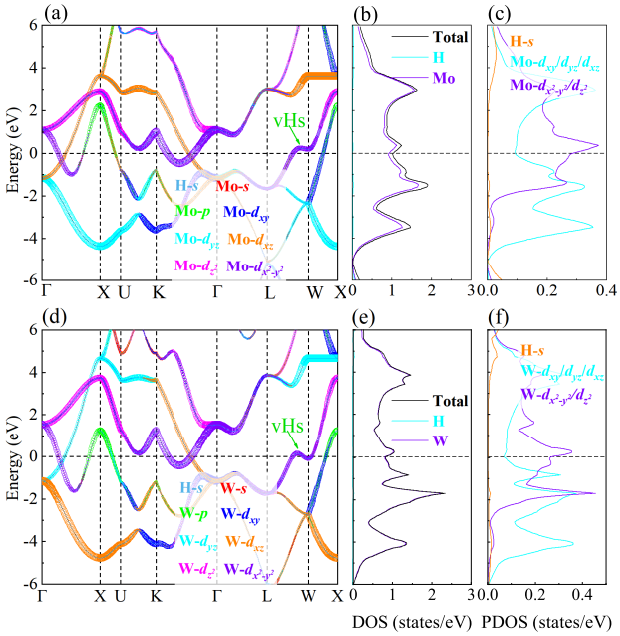

Fig. 2. (a) Orbital-projected band structures for MoH along high-symmetry line Γ-X-U-K-Γ-L-W-X. (b) The total DOS of MoH and the total DOS of Mo and H. (c) PDOS of MoH. (d)-(f) are similar to (a)-(c) but for WH, respectively.

These results confirm that all five MH (M = Mo, W, Ru, Rh, Y) are mechanically stable. Following this, we further investigate the mechanical properties of MH (M = Mo, W, Ru, Rh, Y). Among them, the bulk modulus B, shear modulus G, Young' s modulus E and Poisson' s ratio ν are summarized in Table 1. High values of E, B, and G indicate strong resistance to tensile, compressive, volumetric, and shear deformations, resulting in minimal strain under external stress. ν belongs to typical "positive Poisson's ratio" materials, indicating that the relationship between transverse strain and longitudinal strain conforms to mechanical intuition.

The electron-transfer properties of MH (M = Mo, W, Ru, Rh, Y) can be assessed using the charge den-

sity difference (CDD), which is defined as $\Delta\rho_{MH} = \rho_{MH} - \rho_M - \rho_H$. Among them, ρ_{MH}, ρ_M, and ρ_H represent the charge densities of MH (M = Mo, W, Ru, Rh, Y), isolated M (M = Mo, W, Ru, Rh, Y) and H atoms, respectively. For MoH, the calculated CDD are displayed in Fig. 1(c), and it can be clearly seen that Mo atoms lose electrons and H atoms gain electrons, thus resulting in the formation of Mo-H bonds. The electron localization function (ELF) is displayed in Fig. 1(d), and it indicates that electrons are mainly distributed around the H atoms, suggesting the presence of ionic Mo-H bonds.

Thus, the predicted MH (M = Mo, W, Ru, Rh, Y) exhibit good dynamic, thermodynamic, and mechanical stability. Since MoH and WH exhibit relatively high T_c among the five compounds, we discuss their superconducting and topological properties in detail, while the corresponding results for RuH, RhH, and YH are provided in the Supplemental Material.

Electronic structures. The energy band structures, total DOS, and partial density of states (PDOS) of MoH and WH are shown in Fig. 2. It can be seen that MoH and WH have obvious metallic properties, with three energy bands passing through the Fermi level. The cubic symmetry of MoH and WH leads to highly degenerate energy bands, such as at the high symmetry path Γ-L. Fig. 2(a) shows the energy band orbital projection of MoH along the high-symmetry line Γ-X-U-K-Γ-L-W-X. The energy band at the Fermi level is mainly contributed by Mo-d orbitals. Based on the crystal-field analysis, the d-orbital of Mo splits into two sets of degenerate orbitals, namely the double degenerate d orbital ($d_{x^2-y^2}$ and d_{z^2}) and the triple degenerate d orbital (d_{xy}, d_{xz}, and d_{yz}). The total DOS and PDOS in Figs. 2(b) and 2(c) further illustrate that the DOS at the Fermi level is mainly contributed by double degenerate orbital ($d_{x^2-y^2}$ and d_{z^2}). Notably, at the Fermi level in the L-W directions, there exists a van Hove singularity (vHs) at approximately 0.3 eV. For WH, since Mo and W belong to the same main group, the electronic structures of these two structures are very similar. Fig. 2(d) shows the energy band orbital projection of WH along the same high-symmetry line, with the energy band at the Fermi level mainly contributed by W-d orbitals. The d orbital of W also splits into two sets of degenerate orbitals, double degeneracy and triple degeneracy. The DOS and PDOS of WH are shown in Figs. 2(e) and 2(f). The DOS at the Fermi level is mainly contributed by double degenerate orbital ($d_{x^2-y^2}$ and d_{z^2}) of the W atom. And saddle points at the Fermi level in the L-W direction correspond to the vHs at approximately 0.2 eV in Fig. 2(d) of the band. Although Mo and W have similar atomic radii and belong to the same main group, their band characteristics at vHs differ due to the difference in the main quantum

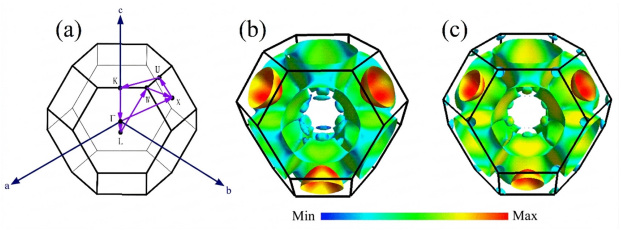

Fig. 3. (a) The first Brillouin zone of MH (M = Mo, W, Ru, Rh, Y) and the high symmetry path Γ-X-U-K-Γ-L-W-X. The FS of (b) MoH and (c) WH with the color drawn proportional to the magnitude of the Fermi velocity ν_F.

number. The 4d orbital of Mo has a small spatial extension and weak interatomic orbital overlap, resulting in strong electronic localization and relatively flat energy bands. On the contrary, W has a 5d orbital with a larger main quantum number, which is more dispersed in space, significantly enhances the integration of atomic orbital overlap, increases electron mobility, and tilts the energy band. To further investigate possible magnetic instabilities, spin-polarized self-consistent calculations were performed for all five MH (M = Mo, W, Ru, Rh, Y) compounds. Within the PBE approximation, all five compounds converge to essentially nonmagnetic states with negligible total magnetic moments. For RhH, additional Hubbard U calculations reveal that its magnetic behavior is sensitive to the effective Hubbard U. The system remains nearly nonmagnetic at small U, while an appreciable spin polarization emerges with increasing U, as shown in Fig. S14 of the Supplemental Material.

Then, we analyse the Fermi surface of MH (M = Mo, W, Ru, Rh, Y). Figs. 3(b) and 3(c) show the FS of MoH and WH, where the colors on the Fermi surface represent the Fermi velocity ν_F,and blue to red indicate that the Fermi velocity is increasing. The formula for calculating Fermi velocity is

$$\nu_F = \frac{\hbar(3\pi^2 n)^{\frac{1}{3}}}{m} \tag{3}$$

where n is the electron number density and m is the effective mass of the electron. The larger the slope of the band (the steeper the band), the greater the Fermi velocity ν_F. Compared with the high symmetry line of the first Brillouin zone in Fig. 3(a), it can be seen that there is a larger Fermi velocity near the high symmetry point X, and a hole pocket is formed, corresponding to the energy band contributed by the p-orbital of Mo atom and W atom at the high symmetry point X in the partial orbital energy band projection of Figs. 2(a) and 2(d).

Topological properties. The electronic band structure of MoH considering spin-orbit coupling (SOC) along the high symmetry direction of Γ-X-U-K-Γ-L-W-X is shown in Fig. 4(a). Among these, the energy bands at the Fermi level are the focus of analy-

sis. Compared with the band structure without SOC in Fig. 2(a), it is found that after introducing SOC, the originally degenerate two energy bands split, thus opening up a global energy gap across the Brillouin zone. The comparison clarifies that SOC mainly lifts degeneracies and opens avoided crossings, while the overall band dispersion and DOS near the Fermi level remain largely unchanged. To further confirm that the relevant bands are isolated throughout the Brillouin zone, we calculated the band gap over the entire Brillouin zone. As shown in Fig. S12 of the Supplemental Material, the gap remains finite throughout the Brillouin zone, confirming that the relevant bands are continuously separated and providing a valid basis for the subsequent $\mathbb{Z}_2$ topological analysis. To characterize the topology of the gap between bands I and II, we calculate the $\mathbb{Z}_2$ topological invariant using the Wannier charge center (WCC) method [51], which has the advantage of universality and is applicable to both centrally symmetric and non centrally symmetric systems. After calculation, any horizontal reference line selected in the $k_x = 0$, $k_y = 0$, and $k_z = 0$ planes intersects the WCC demonstration curve an odd number of times, corresponding to the nontrivial $\mathbb{Z}_2$ index. And selecting any horizontal reference line in the $k_x = 0.5$, $k_y = 0.5$, and $k_z = 0.5$ planes will intersect the WCC demonstration curve an even number of times, corresponding to the trivial $\mathbb{Z}_2$ index. All of this confirms its nontrivial band topology characteristics. Our analysis of the $\mathbb{Z}_2$ topological invariants reveals that this band gap belongs to the strong topological class characterized by the indices (1;000), which unambiguously establishes MoH as a three-dimensional strong topological material. Furthermore, for the sake of supplementary validation, the surface electronic states are calculated. As presented in Fig. 4(b), within the bulk gap caused by SOC, topologically protected surface states can be clearly identified near the Fermi level, further verifying that MoH exhibits a nontrivial topological phase.

For WH, Fig. 4(c) shows the electronic band structures with SOC. There are still two band splits corresponding to the originally degenerate states. We calculated the $\mathbb{Z}_2$ topological invariants of the energy gaps opened by the band splits of band III and band IV. After calculation, any horizontal reference line selected in the $k_x = 0$ and $k_y = 0$ planes intersects the WCC demonstration curve an odd number of times, corresponding to the nontrivial $\mathbb{Z}_2$ index. And any horizontal reference line selected in the $k_x = 0.5$, $k_y = 0.5$, $k_z = 0$, and $k_z = 0.5$ planes intersects the WCC demonstration curve an even number of times, corresponding to the trivial $\mathbb{Z}_2$ index. The above proves that WH is a topologically nontrivial phase. Meanwhile, the surface states of topological protection can be clearly identified within the bulk gap caused by

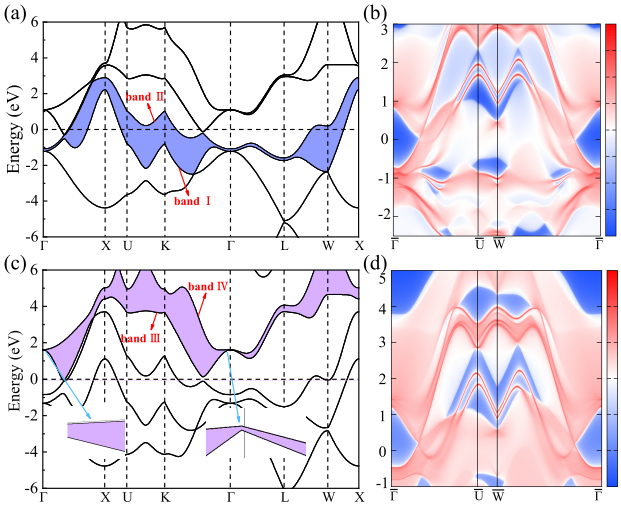

Fig. 4. (a) MoH and (c) WH band structure with SOC. Edge states for (b) MoH and (d) WH. The positive (red end) correspond to higher DOS, and the negative (blue end) denote the bulk band gaps.

SOC near the Fermi level, as shown in Fig. 4(d), thus further verifying that WH exhibits a nontrivial topological phase. Topological surface states can be experimentally probed using angle-resolved photoemission spectroscopy and Shubnikov-de Haas oscillations. A reliable basis for subsequent experimental research is thus established by our theoretical findings, which further suggest that MH (M = Mo, W, Ru, Rh, Y) are competitive candidates for investigating topological superconductivity in the family of rock-salt transition-metal hydrides.

EPC and superconductivity. Considering the metallic properties of MoH and WH, we further explore their possible superconductivity. The phonon spectra weighted by the magnitude of EPC $\lambda_{\mathbf{q}\nu}$ for MoH and WH are shown in Figs. 5(a) and 5(e). Each atom in the primitive cell contributes three degrees of freedom and since the primitive cell of MoH and WH contains two atoms, the phonon spectrum comprises six branches: three acoustic and three optical. The phonon dispersion weighted by the vibration modes of Mo and H, total and atom-projected phonon density of states (PhDOS) are shown in Figs. 5(b) and 5(c). The mass difference between Mo atoms and H atoms is significant, resulting in a large gap between their acoustic and optical branches. The phonon spectrum extends to about 921 cm^{-1}, and the vibration frequency can be divided into two parts: the acoustic mode in the low-frequency range below 205 cm^{-1}, mainly derived from the in-plane and out of plane vibration modes of relatively heavy Mo atoms. The optical modes in the high-frequency range (810 - 921 cm^{-1}) mainly contributed by the in-plane and out of plane vibration modes of relatively light H atoms. Fig. 5(d) shows the Eliashberg spectral function $\alpha^2F(\omega)$

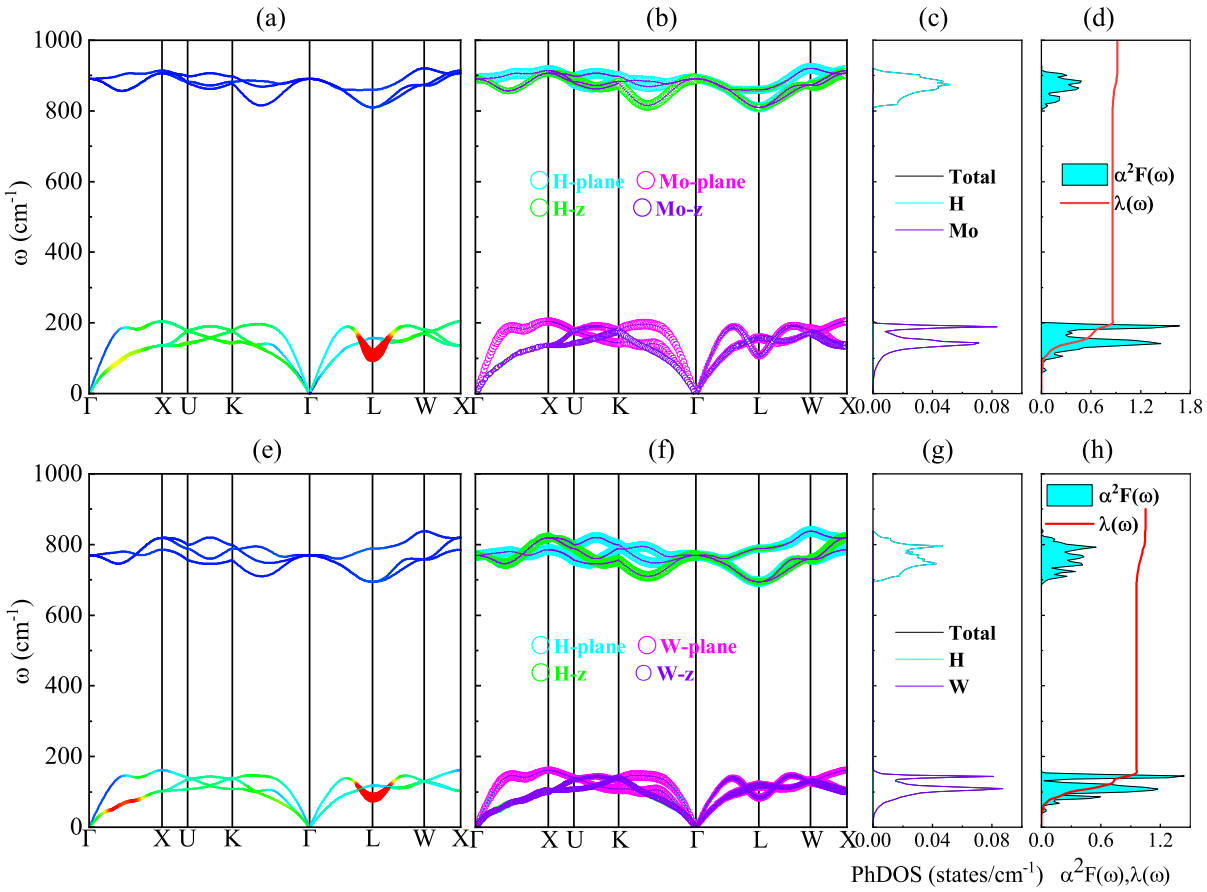

Fig. 5. (a) Phonon dispersion weighted by the magnitude of EPC $\lambda_{\mathbf{q}\nu}$, (b) Phonon dispersion weighted by the vibration modes of Mo and H, (c) total and atom-projected PhDOS, (d) Eliashberg spectral function $\alpha^2F(\omega)$ and cumulative frequency-dependent EPC function $\lambda(\omega)$ for MoH. Here (e)-(h) are similar with (a)-(d) but for WH, respectively.

and cumulative frequency-dependent EPC function $\lambda(\omega)$ of MoH. The vibration mode of Mo contributes about 93% of the total EPC constant ($\lambda = 0.92$), while the vibration mode of H contributes about 7% of the total λ. This indicates that low-frequency phonon modes are the main contributors to EPC. According to the phonon spectrum weighted by the magnitude of EPC $\lambda_{\mathbf{q}\nu}$ as shown in Fig. 5(a), it can be seen that the peak of $\alpha^2F(\omega)$ in Fig. 5(d) corresponds to the soft phonon mode in Fig. 5(a), especially a strong softening mode near the L point of about 140 cm^{-1}, which makes a significant contribution to EPC. The L-point softening is not associated with obvious Fermi-surface nesting (Figs. 3(b) and 3(c)), but coincides with enhanced mode-resolved EPC and peaks of $\alpha^2F(\omega)$. This suggests a Kohn-anomaly-like origin driven by EPC. A quantitative verification via electronic susceptibility is left for future work.

For WH, both phonon characteristics and EPC are extremely similar to MoH, as shown in Figs. 5(e)-5(h). In this system, vibrational contributions separate distinctly by frequency: W atoms dominate the low-frequency range (0 - 162 cm^{-1}), while H vibrations are confined to higher frequencies (694 - 838 cm^{-1}). The vibration mode of W contributes about 91% of the total EPC constant ($\lambda = 1.10$), while the vibration mode of H contributes about 9% of the total λ. The dominant Mo/W contribution to EPC mainly originates from the low-frequency weighting in λ and the dominant Mo/W d states near the Fermi level. In contrast, H-derived electronic states make only a small contribution near the Fermi level, resulting in a weaker EPC contribution. The distribution of strong coupling is also similar to MoH, as shown in Fig. 5(h), with a strong softening mode at approximately 105 cm^{-1} near the L point, which corresponds to the peak of $\alpha^2F(\omega)$ in Fig. 5(h) and makes a significant contribution to EPC, mainly due to the vibration of W atoms. The corresponding phonon vibration modes at the L point are shown in Figs. S10(a) and S10(b) for MoH and WH, respectively. In both compounds, the transition-metal and H atoms vibrate in the same direction, indicating collective lattice vibrations associated with the phonon softening at the L point. Furthermore, the calculated phonon linewidths exhibit pronounced enhancements in the vicinity of

the L point for both MoH and WH, as shown in Figs. S11(a) and S11(b), respectively. The enhanced phonon linewidths indicate strong electron–phonon scattering associated with the softened phonon modes, suggesting that the phonon softening near the L point is closely related to enhanced EPC. Therefore, the superconductivity of MoH and WH mainly comes from the coupling between the double degenerate d-orbital ($d_{x^2-y^2}$ and d_{z^2}) electrons of Mo/W and the softened low-frequency phonons. The bond-oriented nature of these orbitals and their dominant DOS at the Fermi level lead to strong electron-phonon matrix elements. Their T_c are 14.6 K and 14.5 K, respectively. In addition, we also conducted first principles calculations on RuH, RhH and YH, which have properties similar to MoH and WH. Their T_c are 5.3 K, 7.9 K and 4.5 K, respectively, and λ are 0.56, 0.69 and 0.53, respectively. Their calculations are included in the Supplementary Materials.

For RhH, its superconductivity mechanism depends on the strength of U. From the band structure in Fig. S14, we find that $U_c = 0.2$ eV is the critical Hubbard interaction strength for the emergence of itinerant ferromagnetism. For $U \ll U_c$, the system is a paramagnetic metal, in which phonon mediated s-wave superconductivity may still occur. When $U \lesssim U_c$, strong ferromagnetic fluctuations suppress s-wave pairing and may favor p-wave superconductivity. For $U > U_c$, the system becomes a spin polarized ferromagnetic metal. Singlet superconductivity may be strongly suppressed in this regime, yet the possibility of spin triplet superconductivity still remains.

Conclusion. To sum up, we have predicted some new rock-salt type transition-metal hydrides and systematically investigated their electronic, phonon, superconductivity, and topological characteristics. The results show that MH (M = Mo, W, Ru, Rh, Y) exhibit mechanical, dynamical, and thermodynamic stability. The coupling between the double degenerate d-orbital ($d_{x^2-y^2}$ and d_{z^2}) electrons of Mo/W and the softened phonons significantly contributes to their superconductivity. Specifically, the EPC constants for these two compounds are 0.92 and 1.10, respectively, and their T_c stand at 14.6 K and 14.5 K, respectively. When SOC is taken into account, a global energy gap emerges in the energy band structure. Furthermore, by calculating the topological invariant $\mathbb{Z}_2$, we have confirmed that both materials are nontrivial topological materials. Thus, this work offers a valuable platform for exploring the superconducting and topological properties of hydrides under ambient pressure.

Acknowledgements. This work is supported by the National Natural Science Foundation of China (Grant Nos. 12674304, 12074213, 12322402, and 12274206), the Natural Science Foundation of Shandong Province (Grant Nos. ZR2026MS0019 and ZR2023MA082), the Scientific Research Innovation Capability Support Project for Young Faculty (SRICSPYF-ZY2025164), the National Key R&D Program of China (2024YFA1410500, 2022YFA1403601), the Natural Science Foundation of Jiangsu Province (No.BK20233001), and the Fundamental Research Funds for the Central Universities (KG202501).

References

[1] Huang Y Y 2025 (*Preprint* 2408.00202)

[2] Sun Y, Zhong Z C, Shirakawa T, Franchini C, Li D Z, Li Y Y, Yunoki S J, and Chen X Q 2013 *Phys. Rev. B* **88** 235122

[3] Hsieh T H, Lin H, Liu J W, Duan W H, Bansil A, and Fu L 2012 *Nat. Commun.* **3** 982

[4] Liu Z K, Zhou B, Zhang Y, Wang Z J, Weng H M, Prabhakaran D, Mo S K, Shen Z X, Fang Z, Dai X, Hussain Z, and Chen Y L 2014 *Science* **343** 864–867

[5] Wang Z J, Weng H M, Wu Q S, Dai X, and Fang Z 2013 *Phys. Rev. B* **88** 125427

[6] Sur S and Setty C 2025 *Phys. Rev. Res.* **7** 013280

[7] Wang Z J, Sun Y, Chen X Q, Franchini C, Xu G, Weng H M, Dai X, and Fang Z 2012 *Phys. Rev. B* **85** 195320

[8] Ruan J W, Jian S K, Yao H, Zhang H J, Zhang S C, and Xing D Y 2016 *Nat. Commun.* **7** 11136

[9] Lv B Q, Weng H M, Fu B B, Wang X P, Miao H, Ma J, Richard P, Huang X C, Zhao L X, Chen G F, Fang Z, Dai X, Qian T, and Ding H 2015 *Phys. Rev. X* **5** 031013

[10] Li Y 2025 *ACS Omega* **10** 7973–7980

[11] Wang Z J, Wieder B J, Li J, Yan B H, and Bernevig B A 2019 *Phys. Rev. Lett.* **123** 186401

[12] Yan D Y, Geng D Y, Gao Q, Cui Z H, Yi C J, Feng Y, Song C Y, Luo H L, Yang M, Arita M, Kumar S, Schwier E F, Shimada K, Zhao L, Wu K H, Weng H M, Chen L, Zhou X J, Wang Z J, Shi Y G, and Feng B J 2020 *Phys. Rev. B* **102** 205117

[13] Shang T, Zhao J Z, Gawryluk D J, Shi M, Medarde M, Pomjakushina E, and Shiroka T 2020 *Phys. Rev. B* **101** 214518

[14] Yan D Y, Yang M, Wang C X, Song P B, Yi C J, and Shi Y G 2021 *Supercond. Sci. Technol.* **34** 035025

[15] Huang A, Smith A D, Schwinn M, Lu Q S, Chang T R, Xie W W, Jeng H T, and Bian G 2018 *Phys. Rev. Mater.* **2** 054205

[16] Babu K R and Guo G Y 2019 *Phys. Rev. B* **99** 104508

[17] Allen P B and Dynes R C 1975 *Phys. Rev. B* **12** 905–922

[18] McMillan W L 1968 *Phys. Rev.* **167** 331–344

[19] Moussa J E and Cohen M L 2006 *Phys. Rev. B* **74** 094520

[20] Yang L, Li Y P, Liu H D, Jiao N, Ni M Y, Lu H Y, Zhang P, and Ting C S 2023 *Chin. Phys. Lett.* **40** 017402

[21] Ding H, Sui C H, Wan Y, Han Y L, Jiao N, Lu H Y, and Zhang P 2026 *J. Phys. Chem. C* **130** 1785–1790

[22] Li Y P, Yang L, Liu H D, Jiao N, Ni M Y, Hao N, Lu H Y, and Zhang P 2022 *Phys. Chem. Chem. Phys.* **24** 9256–9262

[23] Han Y L, Li Y P, Yang L, Liu H D, Jiao N, Wang B Y, Lu H Y, and Zhang P 2023 *Mater. Today Phys.* **30** 100954

[24] Han Y L, Liu H D, Jiao N, Zheng M M, Lu H Y, Wang B T, and Zhang P 2023 *Phys. Rev. Mater.* **7** 114802

[25] Tanaka K, Tse J S, and Liu H 2017 *Phys. Rev. B* **96** 100502

[26] Strobel T A, Ganesh P, Somayazulu M, Kent P R C, and Hemley R J 2011 *Phys. Rev. Lett.* **107** 255503

[27] Duan D, Liu Y X, Tian F B, Li D, Huang X L, Zhao Z L, Yu H Y, Liu B B, Tian W J, and Cui T 2014 *Sci. Rep.* **4** 6968

[28] Drozdov A P, Eremets M I, Troyan I A, Ksenofontov V, and Shylin S I 2015 *Nature* **525** 73–76

[29] Somayazulu M, Ahart M, Mishra A K, Geballe Z M, Baldini M, Meng Y, Struzhkin V V, and Hemley R J 2019 *Phys. Rev. Lett.* **122** 027001

[30] Drozdov A P, Kong P P, Minkov V S, Besedin S P, Kuzovnikov M A, Mozaffari S, Balicas L, Balakirev F F, Graf D E, Prakapenka V B, Greenberg E, Knyazev D A, Tkacz M, and Eremets M I 2019 *Nature* **569** 528–531

[31] Hong F, Yang L X, Shan P F, Yang P T, Liu Z Y, Sun J P, Yin Y Y, Yu X H, Cheng J G, and Zhao Z 2020 *Chin. Phys. Lett.* **37** 107401

[32] Grockowiak A D, Ahart M, Helm T, Coniglio W A, Kumar R, Glazyrin K, Garbarino G, Meng Y, Oliff M, Williams V, Ashcroft N W, Hemley R J, Somayazulu M, and Tozer S W 2022 *Front. Electron. Mater.* **2** 837651

[33] Liu H Y, Naumov I I, Hoffmann R, Ashcroft N W, and Hemley R J 2017 *Proc. Natl. Acad. Sci. USA* **114** 6990–6995

[34] Peng F, Sun Y, Pickard C J, Needs R J, Wu Q, and Ma Y M 2017 *Phys. Rev. Lett.* **119** 107001

[35] Li Y W, Hao J, Liu H Y, Tse J S, Wang Y C, and Ma Y M 2015 *Sci. Rep.* **5** 9948

[36] Wang Y Y, Wang K, Sun Y, Ma L, Wang Y C, Zou B, Liu G T, Zhou M, and Wang H B 2022 *Chin. Phys. B* **31** 106201

[37] Jiang K Y, Chen Y J, and Lu H Y 2024 *J. Appl. Phys.* **136** 023903

[38] Li X X, Xu W S, Zhou Z G, Shi J M, Liu H Y, Fang Y W, Cui W W, Li Y W, and Marques M A L 2025 (*Preprint* 2511.04222)

[39] Giannozzi P, Baroni S, Bonini N, Calandra M, Car R, Cavazzoni C, Ceresoli D, Chiarotti G L, Cococcioni M, Dabo I, Dal Corso A, de Gironcoli S, Fabris S, Fratesi G, Gebauer R, Gerstmann U, Gougoussis C, Kokalj A, Lazzeri M, Martin-Samos L, Marzari N, Mauri F, Mazzarello R, Paolini S, Pasquarello A, Paulatto L, Sbraccia C, Scandolo S, Sclauzero G, Seitsonen A P, Smogunov A, Umari P, and Wentzcovitch R M 2009 *J. Phys.: Condens. Matter* **21** 395502

[40] Taylor J, Guo H, and Wang J 2001 *Phys. Rev. B* **63** 245407

[41] Blöchl P E 1994 *Phys. Rev. B* **50** 17953–17979

[42] Kresse G and Joubert D 1999 *Phys. Rev. B* **59** 1758–1775

[43] Perdew J P, Burke K, and Ernzerhof M 1996 *Phys. Rev. Lett.* **77** 3865–3868

[44] Baroni S, de Gironcoli S, Dal Corso A, and Giannozzi P 2001 *Rev. Mod. Phys.* **73** 515–562

[45] Lopez Sancho M P, Lopez Sancho J M, Sancho J M L, and Rubio J 1985 *J. Phys. F: Metal Phys.* **15** 851

[46] Wu Q S, Zhang S N, Song H F, Troyer M, and Soluyanov A A 2018 *Comput. Phys. Commun.* **224** 405

[47] Souza I, Marzari N, and Vanderbilt D 2001 *Phys. Rev. B* **65** 035109

[48] Marzari N, Mostofi A A, Yates J R, Souza I, and Vanderbilt D 2012 *Rev. Mod. Phys.* **84** 1419–1475

[49] Franchini C, Kováčik R, Marsman M, Sathyanarayana Murthy S, He J, Ederer C, and Kresse G 2012 *J. Phys.: Condens. Matter* **24** 235602

[50] Mouhat F and Coudert F X 2014 *Phys. Rev. B* **90** 224104

[51] Soluyanov A A and Vanderbilt D 2011 *Phys. Rev. B* **83** 235401